# Wideband Arrhythmia-Insensitive-Rapid (AIR) Pulse Sequence for Cardiac $T_1$ mapping without Image Artifacts induced by ICD

**KyungPyo Hong**[1,2], **Eun-Kee Jeong**[2], **T. Scott Wall**[3], **Stavros G. Drakos**[3], and **Daniel Kim**[2]

[1]Department of Bioengineering, University of Utah, Salt Lake City, UT

[2]UCAIR, Department of Radiology, University of Utah, Salt Lake City, UT

[3]Division of Cardiology, Internal Medicine, University of Utah, Salt Lake City, UT

## Abstract

**Purpose**—To develop and evaluate a wideband arrhythmia-insensitive-rapid (AIR) pulse sequence for cardiac $T_1$ mapping without image artifacts induced by implantable-cardioverter-defibrillator (ICD).

**Methods**—We developed a wideband AIR pulse sequence by incorporating a saturation pulse with wide frequency bandwidth (8.9 kHz), in order to achieve uniform $T_1$ weighting in the heart with ICD. We tested the performance of original and "wideband" AIR cardiac $T_1$ mapping pulse sequences in phantom and human experiments at 1.5T.

**Results**—In 5 phantoms representing native myocardium and blood and post-contrast blood/tissue $T_1$ values, compared with the control $T_1$ values measured with an inversion-recovery pulse sequence without ICD, $T_1$ values measured with original AIR with ICD were considerably lower (absolute percent error >29%), whereas $T_1$ values measured with wideband AIR with ICD were similar (absolute percent error <5%). Similarly, in 11 human subjects, compared with the control $T_1$ values measured with original AIR without ICD, $T_1$ measured with original AIR with ICD was significantly lower (absolute percent error >10.1%), whereas $T_1$ measured with wideband AIR with ICD was similar (absolute percent error <2.0%).

**Conclusion**—This study demonstrates the feasibility of a wideband pulse sequence for cardiac $T_1$ mapping without significant image artifacts induced by ICD.

## Keywords

sudden cardiac death; ICD; wideband; cardiac $T_1$ mapping; ECV; myocardial fibrosis; heart failure

## Introduction

Heart failure (HF) is a major healthcare problem that affects over 5 million Americans (1). Patients with advanced or end-stage HF (i.e., stage D according to the ACCF/AHA

classification (2)) are characterized by marked symptoms at rest despite maximal medical therapy (3); consequently, they have a 1-year mortality rate of approximately 40–50% (4, 5). While heart transplantation is a well-established treatment for improving both survival and quality of life for these patients (6), from healthcare's perspective, it is unsustainable due to a continuing shortage of donor hearts (7). To address this imbalance, the 2013 ACC/AHA guideline (2) recommends left ventricular (LV) assist device (LVAD) (8–11) as a destination therapy (12, 13) in select patients. Unfortunately, current clinical risk scores and profiles provide poor discrimination between responders and non-responders to LVAD therapy.

Cardiac fibrosis, as a marker of adverse structural remodeling, is a strong predictor of functional response to intervention (14). While myocardial biopsy is the current gold standard for assessment of fibrosis, it is rarely indicated due to its associated non-negligible risk of complications and susceptibility to sampling errors. MRI is emerging as a reliable non-invasive test for myocardial biopsy (15) using cardiac $T_1$ mapping (16–18) or extracellular volume (ECV) fraction (18–24) mapping pulse sequences. Unlike myocardial biopsy, these MRI methods provide a means to sample the whole heart non-invasively. In the context of HF induced by non-ischemic cardiomyopathy, cardiac $T_1$ and ECV fraction mapping pulse sequences may be better than late gadolinium-enhanced (LGE) MRI for quantification of myocardial fibrosis burden.

Because LVAD candidates (i.e., end-stage HF) typically have prophylactic implantable cardioverter-defibrillator (ICD) for prevention of sudden cardiac death and/or arrhythmia, a new pulse sequence needs to be developed to reduce measurement error due to ICD and/or arrhythmia. Despite the fact that MRI can be performed safely in most patients with cardiac devices at 1.5T (25, 26), many patients who would derive benefit from MRI do not undergo MRI largely due to image artifacts arising from the ICD generator. Recently, the feasibility of wideband LGE MRI was demonstrated for assessment of focal fibrosis in patients with ICD (27–29), where "wideband" refers to the modified hyperbolic secant radio-frequency (RF) pulse used to invert the magnetization in the presence of ICD. To our knowledge, no other study has reported successful cardiac $T_1$ mapping without image artifacts induced by ICD.

Among the different cardiac $T_1$ mapping pulse sequences, an arrhythmia-insensitive-rapid (AIR) cardiac $T_1$ mapping pulse sequence (30) with a short scan time (~2–3 heart beats) is well suited for imaging patients with advanced HF, because they often have rapid heart rates and/or irregular heart rhythm and/or limited breath-hold capacity. In this study, we will extend AIR cardiac $T_1$ mapping to be insensitive to ICD, by incorporating a saturation RF pulse with wide frequency bandwidth to achieve uniform $T_1$ weighting in the heart with ICD. We demonstrate the feasibility of wideband AIR cardiac $T_1$ mapping and evaluate its relative accuracy in phantom and human experiments at 1.5T.

# Methods

## Saturation Pulse Modules

As previously described in (30), the original AIR cardiac $T_1$ mapping pulse sequence was implemented with balanced steady-state free precession (b-SSFP) readout. This pulse sequence acquires two single-shot images, $T_1$-weighted and proton density (PD), within a scan time of 2–3 cardiac cycles, depending on heart rate. To minimize image artifacts induced by ICD and enable successful imaging of patients with ICD implantation, we modified the original AIR pulse sequence to use ultra-fast gradient echo (TurboFLASH, Siemens; FastSPGR, GE; TFE, Philips) readout. We used the vendor's saturation pulse module for original AIR, which is comprised of three 90° rectangular pulses with 0.5 ms duration for each rectangular RF pulse (see Figure 1A in (31)). We used this modified AIR pulse sequence (i.e., TurboFLASH readout + vendor saturation pulse module) as a reference to compare the wideband AIR pulse sequence described below. For clarity, we refer to this modified AIR as original AIR throughout this report.

ICD generator is typically implanted on the patient's left shoulder, approximately 5–10 cm away from the heart. This distance will induce a center frequency shift as large as 2–6 kHz (27). Standard saturation pulse modules have relatively low frequency bandwidth and, therefore, are unsuitable for complete saturation of magnetization in the presence of ICD. This means that an effective saturation RF pulse for wideband AIR cardiac $T_1$ mapping in patients with ICD should have a frequency bandwidth greater than 6 kHz to achieve uniform $T_1$ weighting. One promising RF pulse module that can effectively saturate the magnetization over a wide range of frequencies is RF field ($B_1$) insensitive train to obliterate signal (BISTRO) (32), which was originally developed for outer volume suppression in inhomogeneous $B_1$. The primary concept behind BISTRO is to not meet the adiabatic condition on purpose for each individual inversion RF pulse (i.e., < 180° excitation per pulse), but ultimately fully rotate the longitudinal magnetization ($M_z$) onto the transverse plane (i.e., net excitation equal to 90°) with a train of sub-optimal inversion RF pulses, where key design considerations are the number of pulses, frequency bandwidth, total pulse duration, and specific absorption rate (SAR). Figure 1 shows the pulse sequence diagram of BISTRO that was incorporated into AIR. See Appendix for more details on our implementation of BISTRO. For clarity, AIR with BISTRO is referred to as wideband AIR throughout this report.

## Calculation of RF Energy Deposition by the Saturation Pulse Modules

Using the pulse sequence simulator (IDEA, Siemens Healthcare, Erlangen, Germany), we calculated the transmit RF energy for each saturation pulse module, assuming that the RF voltage needed to achieve $B_1+$ (normalized by gyromagnetic ratio) of 500 Hz is 300–350 V. This RF calibration assumption at 1.5T is consistent with results reported in (33). Nominal $B_1+$ (normalized by gyromagnetic ratio) is 500 Hz (300–350 V) for the original saturation pulse module, whereas nominal $B_1+$ (normalized by gyromagnetic ratio) is 926 Hz (556–648 V) for the wideband saturation pulse module. Note the RF amplifier of our Siemens Espree system delivers a maximum voltage of 949 V. At these settings, theoretically calculated transmit RF energy of original and wideband saturation pulse modules was 3.7

and 101.0 J, respectively. These energy deposition values translate to whole-body SAR of approximately 0.125 and 0.5 W/kg for original and wideband AIR $T_1$ mapping acquisitions, respectively, depending on subject size. We note that this SAR calculation includes saturation pulse and RF excitations for PD and $T_1$-weighted image acquisitions. This theoretical analysis confirms that whole-body SAR induced by wideband AIR is 3–4 times lower than the safe limits (1.5–2 W/kg) recommended by established pacemaker/ICD MRI protocols at 1.5T (25, 26).

### Calculation of Frequency Bandwidth of the Saturation Pulse Modules

We determined empirically, in a phantom positioned near magnet isocenter, frequency bandwidth of the original and wideband saturation pulse modules. Compared with original AIR, wideband AIR had 256% higher frequency bandwidth (full width at half maximum [FWHM] = 2.5 kHz and 8.9 kHz for original and wideband, respectively). For more details on the methods and results, see Appendix and Figure 2A. This experimental analysis confirms that wideband AIR is insensitive to center frequency shift expected with ICD located 5–10 cm away from the heart.

### MRI Protocol

The original and wideband AIR cardiac $T_1$ mapping pulse sequences were implemented on a 1.5T whole-body MRI scanner (Espree, Siemens Healthcare, Erlangen, Germany), equipped with a gradient system capable of achieving a maximum gradient strength of 33 mT/m and a slew rate of 100 T/m/s. RF excitation was performed using the body coil, and an 8-element coil array was used for signal reception.

Both original and wideband AIR pulse sequences used the following relevant imaging parameters: field of view = 360 mm × 270 mm (phase-encoding), acquisition matrix = 128 × 96 (phase-encoding), in-plane resolution = 2.8 mm × 2.8 mm, slice thickness = 8 mm, echo time (TE) = 1.1 ms (asymmetric readout), repetition time (TR) = 2.2 ms, receiver bandwidth = 1000 Hz/pixel, center-out k-space ordering, readout duration = 132 ms, saturation-recovery time delay (TD) = 600 ms, flip angle = 10°, breath-hold duration = 2–3 heart beats, and generalized autocalibrating partially parallel acquisitions (GRAPPA) (34) with an acceleration factor = 1.6 (including reference lines). Note that in center-out k-space ordering the first RF excitation is used to acquire the origin of k-space. This acquisition scheme minimizes the sensitivity to excitation angle variation (35, 36) and enables straight-forward calculation of $T_1$ using the Bloch equation describing ideal saturation-recovery, as previously described (30).

### Experiment 1: Evaluation of Sensitivity to ICD and Intracardiac Leads in Phantom

We evaluated the performance of original and wideband AIR pulse sequences with and without an ICD generator (Vitality AVT Model A155, GUIDANT Boston Scientific, Natick, Massachusetts) taped to one side of the phantom as shown in Figure 3. We performed $T_1$ mapping in a coronal plane with the ICD in the plane, in order to visualize the effectiveness of the saturation pulse modules as a function of ICD distance. We also performed a static magnetic field ($B_0$) mapping acquisition (i.e., double echo with TE difference = 4.76 ms) with matching spatial resolution as $T_1$ mapping. For cases with ICD, the $B_0$ maps were

generated after performing phase unwrapping based on network programming (37). The same experiment was repeated with intracardiac leads attached to the same location. In this experiment, original AIR cardiac $T_1$ mapping without ICD was used as the control.

## Experiment 2: Evaluation of Accuracy in MnCl$_2$ Phantoms with ICD

We tested the performance of original and wideband AIR cardiac $T_1$ mapping pulse sequences in phantoms with clinically relevant $T_1$ and $T_2$ values positioned near magnet isocenter. Specifically, we imaged five phantoms with different concentrations of manganese (II) chloride (MnCl$_2$) in distilled water (see Table 1 for the concentration and reference $T_1$ and $T_2$ values). MnCl$_2$ was chosen because it has $T_1/T_2 \approx 10$ at 1.5 T (38), which is comparable to that of tissues.

Reference $T_1$ values were measured using an inversion-recovery fast spin echo (IR-FSE) pulse sequence; the resulting data were analyzed using a 2-parameter fit of the mono-exponential signal relaxation, solving for equilibrium signal amplitude and $T_1$. The relevant imaging parameters for IR-FSE include: same spatial resolution as AIR, excitation flip angle = 90°, refocusing flip angle = 180°, TE = 6 ms, TR = 20 s (> 5 $T_1$s), receiver bandwidth = 501 Hz/pixel, turbo factor = 7, and number of images = 16. The inversion times were 100, 200, 300, 400, 500, 600, 700, 800, 1000, 1100, 1200, 1500, 1800, 2300, 2700, and 20000 ms.

For comparison, we also performed 3-3-5 modified Look-Locker inversion recovery (MOLLI)(39) with b-SSFP readout and heart rate simulated to 60 beats per minute. The relevant imaging parameters for 3-3-5 MOLLI include: same spatial resolution as AIR, scan time = 17 heart beats, flip angle = 35°, TE = 1.1 ms, TR = 2.6 ms, receiver bandwidth = 930 Hz/pixel, and inversion times and linear k-space ordering as previously described (39).

Reference $T_2$ values were measured using a multi-echo fast spin echo (ME-FSE) pulse sequence (40); the resulting data were analyzed using a 3-parameter fit of the mono-exponential signal relaxation, solving for initial signal amplitude, $T_2$, mean background noise. The relevant imaging parameters for ME-FSE include: same spatial resolution as AIR, excitation flip angle = 90°, refocusing flip angle = 180°, TR = 20 s (> 5 $T_1$s), receiver bandwidth = 501 Hz/pixel, turbo factor = 2, inter-echo spacing = 4.7 ms, inter-image spacing = 9.4 ms, and number of images = 12. The image echo times were 9.4, 19, 28, 38, 47, 57, 66, 76, 85, 95, 104, and 113 ms.

For each phantom vial, with the ICD generator taped 10 cm away from the phantom vial (through-plane direction), we performed original and wideband AIR $T_1$ mapping acquisitions. This experiment was repeated without ICD for completeness.

## Experiment 3: Evaluation of Accuracy in MnCl$_2$ Phantoms as a Function of Center Frequency Shift

We evaluated the performance of original and wideband AIR in phantoms (same as *Experiment 2*) as a function of center frequency shift (same setup as the *Frequency Bandwidth* experiment; see Appendix).

### Experiment 4: Evaluation of Accuracy in Human Subjects with ICD

Human imaging was conducted in accordance with protocols approved by our institutional Review Board and the Health Insurance Portability and Accountability Act; all subjects provided written informed consent.

We evaluated the performance of original and wideband AIR cardiac $T_1$ mapping pulse sequences in 11 human volunteers (10 males, 1 female, mean age = $30.0 \pm 6.0$ years) without prior history of heart disease. In each subject, we conducted $T_1$ mapping in 2-chamber and short-axis planes of the left ventricle, without administration of contrast agent (i.e., native $T_1$ mapping). To mimic image artifacts induced by ICD, we taped the ICD generator on each subject's left shoulder, approximately 5–10 cm superior to the left nipple, and performed original and wideband AIR cardiac $T_1$ mapping acquisitions. This mimicking approach (taping an ICD on left shoulder) was first established by Rashid et al. at 1.5T (27) and verified by our group at 3T (29). In human experiments, original AIR cardiac $T_1$ mapping without ICD was used as the control (see phantom results in Table 1 for justification).

In one male volunteer (age = 37), we performed native and post-contrast (15 and 35 min after administration of 0.15 mmol/kg of MultiHance) cardiac $T_1$ mapping in a 2-chamber plane of the left ventricle. This experiment was conducted to verify insensitivity to clinically relevant $T_2$. For each time point (baseline and 15 and 35 min after administration of MultiHance), we performed original and wideband AIR $T_1$ mapping with and without ICD, for a total of 4 AIR $T_1$ mapping acquisitions (original AIR, original AIR with ICD, wideband AIR, and wideband AIR with ICD) per time point. For each time point, we first randomized the ICD presence, and then randomized the pulse sequence order. To further reduce the impact of contrast agent washout effects, we streamlined the protocol to perform 4 $T_1$ mapping acquisitions per time point in 1 min (including breathing instructions), while making sure to allow full magnetization recovery between acquisitions (i.e., wait time > 5 $T_1$s). To maintain the same ICD position throughout MRI at different time points, we drew the contour of the ICD on the volunteer's chest for repeatable taping and removal.

### Image Analysis

To achieve noise reduction during post-processing, which is important since low signal-to-noise ratio is expected with ultra-fast gradient echo readout and 10° flip angle, we applied a modified Hanning window to the k-space representation of each image. To estimate the blurring effects of the Hanning window, we calculated its point spread function (PSF) as the inverse Fourier transform of the window. We then calculated the FWHM with subpixel precision using linear interpolation. The resulting FWHM was 1.5 and 1.3 pixel in the frequency-encoding and phase-encoding directions, respectively. Note that FWHM of an ideal PSF is 1 pixel.

For calculation of $T_1$, the $T_1$-weighted image was divided by the corresponding PD image on a pixel-by-pixel basis, and the ratio was used to calculate $T_1$ based on the Bloch equation describing $T_1$ relaxation in ideal saturation-recovery, as previously described (30). For the phantom experiments, we generated a mask defining the phantom boundary based on

intensity thresholding to remove the background and include only the whole phantom. For cardiac data analysis, endo- and epi-cardial contours were manually drawn to segment the myocardium, and another region-of-interest (ROI) was drawn to encircle the LV cavity. Care was taken to avoid partial volume averaging for each contour tracing (see Figure 4). All image processing was conducted using customized software programmed in Matlab (R2009a, The MathWorks, Inc., Natick, MA).

### Statistical Analysis

For statistical analysis of human data from 11 subjects, for each measurement type (native blood, native myocardium) per cardiac plane (short-axis, 2-chamber view), the mean $T_1$ value within an ROI (blood or myocardium) was pooled and averaged over 11 subjects. For each measurement type per cardiac plane, a single-factor analysis of variance was used to compare the mean $T_1$ values between four groups (original AIR without ICD, original AIR with ICD, wideband AIR without ICD, and wideband AIR with ICD), and Bonferroni correction was used to compare the mean values between the control (original AIR without ICD) and other three groups (original AIR with ICD, wideband AIR without ICD, and wideband AIR with ICD). A $p < 0.05$ was considered to be significant. All statistical analyses were performed using the Analyse-it software (Analyse-it Software, Ltd., Leeds, United Kingdom).

## Results

### Experiment 1: Evaluation of Sensitivity to ICD and Intracardiac Leads in Phantom

Figure 3 shows coronal $T_1$ maps of a phantom with ICD taped on one side of the phantom as shown. A $T_1$ map acquired with original AIR without ICD is also shown as a reference. Original AIR with ICD yielded considerable image artifacts, whereas wideband AIR with ICD suppressed image artifacts in regions as shown. Figure 3 also shows the corresponding $T_1$ maps with intracardiac leads attached to the same location as ICD. Note that both original and wideband AIR were insensitive to intracardiac leads. The corresponding $B_0$ maps confirm that ICD distorts $B_0$ significantly, where the peak center frequency offset is approximately 1,700 Hz. We note that regions close to the ICD (presumably with even higher frequency offset) were removed because of signal dropout. For completeness, see the corresponding plots of $T_1$ as a function of center frequency offset on a pixel-by-pixel basis (Supporting Figure S1).

### Experiment 2: Evaluation of Accuracy in MnCl$_2$ Phantoms with ICD

In 5 phantoms with different concentrations of $MnCl_2$, compared with the control $T_1$ values derived from IR-FSE without ICD, the corresponding $T_1$ values were considerably lower for original AIR with ICD, whereas the $T_1$ values were similar for wideband AIR with ICD. For completeness, see the corresponding $T_1$ results for original and wideband AIR and MOLLI without ICD (Table 1). We note that the standard deviation per phantom is considerably higher for original AIR with ICD than wideband AIR with ICD, implying higher sensitivity to ICD for original AIR.

### Experiment 3: Evaluation of Accuracy in MnCl$_2$ Phantoms as a Function of Center Frequency Shift

Figure 2B shows plots of T$_1$ as a function of center frequency shift. Consistent with the frequency bandwidth experiment, wideband AIR produced consistent T$_1$ results over 8.9 kHz, whereas original AIR produced consistent T$_1$ results over 2.5 kHz.

### Experiment 4: Evaluation of Accuracy in Human Subjects with ICD

Figure 4 shows representative native T$_1$ maps in short-axis and long-axis planes of the heart of two different volunteers. Compared with original AIR without ICD as the control, original AIR with ICD produced less accurate T$_1$ results, whereas wideband AIR with ICD produced more accurate T$_1$ results. For completeness, see the corresponding T$_1$ results for original and wideband AIR without ICD (Supporting Table S1). We note that the standard deviation per ROI is considerably higher for original AIR with ICD than wideband AIR with ICD, implying higher sensitivity to ICD for original AIR.

Averaging the results over 11 human subjects, the mean myocardial and blood T$_1$ measurements were significantly different between the four groups (Table 2; $p < 0.001$). Compared with original AIR without ICD as the control, only original AIR with ICD was significantly different in both imaging planes ($p < 0.05$). We note that native T$_1$ measurements (myocardial T$_1$ ~ 1,100 ms; blood T$_1$ ~ 1,500 ms) made with original AIR without ICD and wideband AIR with and without ICD are comparable to ex-vivo (41) and in vivo (42) myocardial and blood T$_1$ measurements at 1.5T reported in literature.

Figure 5 shows native and post-contrast T$_1$ maps of another volunteer. Similar to the results shown in Figure 4 and data summarized in Table 1, compared with original AIR without ICD, original AIR with ICD produced less accurate T$_1$ results, whereas wideband AIR with ICD produced more accurate T$_1$ results. For completeness, see the corresponding T$_1$ results for original and wideband AIR without ICD (Supporting Table S2). Consistent with phantom and native cardiac T$_1$ results, the standard deviation per ROI is considerably higher for original AIR with ICD than wideband AIR with ICD, implying higher sensitivity to ICD for original AIR.

## Discussion

This study demonstrates the feasibility of a wideband pulse sequence for cardiac T$_1$ mapping without significant image artifacts induced by ICD at 1.5T. In both phantom and human experiments, compared with control T$_1$ measurements without ICD, original AIR with ICD produced less accurate T$_1$ results, whereas wideband AIR with ICD produced more accurate T$_1$ results.

This study has several points that warrant discussion. First, to our knowledge, this is the first study reporting successful cardiac T$_1$ mapping without significant image artifacts induced by ICD. Future studies include evaluation of diffuse myocardial fibrosis burden in patients with ICD implantation. Second, in addition to the image artifacts that cause T$_1$ error, ICD may also cause severe image distortion, spatial shifts, and signal loss due to intravoxel dephasing, all of which may be a problem when registering different MR images which have different

sensitivities. These effects can be minimized by using a readout with short echo time such as ultra-short TE pulse sequences. Third, compared with original AIR, wideband AIR deposits more energy per unit time (i.e., higher SAR). However, in the context of wideband AIR cardiac $T_1$ mapping (one PD image acquisition without saturation pulse and one $T_1$-weighted image acquisition with saturation pulse, each acquisition with TurboFLASH readout), we were able to perform wideband AIR safely; it produces whole-body SAR of 0.5 W/kg, which is 3–4 times lower than the safe limits (1.5–2 W/kg) recommended by established pacemaker/ICD MRI protocols at 1.5T (25, 26). Therefore, it is highly unlikely that wideband AIR will cause significant lead tip heating. Nevertheless, a future comprehensive study is warranted to measure RF-induced lead tip heating with wideband AIR, similar to (43, 44). Fourth, this study did not test other investigational cardiac $T_1$ mapping pulse sequences in the presence of ICD. Other investigational cardiac $T_1$ mapping pulse sequences (MOLLI (39) and shMOLLI (45) using a standard hyperbolic secant adiabatic inversion RF pulse; SASHA (42) and MLLSR (46) using a standard saturation pulse) are likely to be sensitive to ICD and produce inaccurate $T_1$ results, because the frequency bandwidth of the aforementioned RF pulse modules is not wide enough to handle the large center frequency shift induced by ICD. In addition, MOLLI, shMOLLI, MLLSR, and SASHA all use b-SSFP, so the readout will also generate image artifacts induced by ICD. Therefore, we did not compare wideband AIR with MOLLI, shMOLLI, MLLSR, and SASHA, since their wideband counterparts are currently unavailable. A head-to-head comparison between wideband AIR to wideband versions of MOLLI, shMOLLI, MLLSR, and SASHA (which currently do not exist) is beyond the scope of this study. Fifth, we note that both original (FWHM = 2.5 kHz) and wideband (FWHM = 8.9 kHz) saturation pulse modules are insensitive to typical static magnetic field inhomogeneity in the heart at 1.5T (~ 100 Hz, largely due to the heart-lung interface and/or cardiac veins)(47). Sixth, while duration of the wideband pulse module is 151 ms, the total RF time is only 46 ms, whereas the remaining time is used to play crusher and spoiler magnetic field gradients. We note that in the context of saturation of magnetization, $T_2$ relaxation during the RF time is a benefit, whereas in the context of inversion of magnetization $T_2$ relaxation is a detriment. Therefore, BISTRO is insensitive to $T_2$ in the context of saturation recovery of magnetization (see Table 1 and Figure 5). Seventh, our implementation of BISTRO differs from the original version (32); the latter was designed for high field applications. In contrast, our application is largely restricted to 1.5T because of unknown safety associated with MRI of patients with ICD implantation at 3T. $B_1+$ variation within the heart at 1.5T is approximately 10% (48); therefore, in the context of MRI of patients with ICD implantation, $B_1+$ variation is less of a concern than static magnetic field variation induced by ICD, as previously described (27). We had conducted a preliminary experiment to compare the performance of BISTRO between constant and variable RF amplitudes, but did not observe a significant difference between them. Therefore, for ease of implementation, we elected to design BISTRO with constant RF amplitudes. We also performed a preliminary test to compare the level of stimulated echoes between constant and variable durations of crusher gradients, and noticed that varying the durations produced less stimulated echoes in the context of TurboFLASH readout.

This study has three limitations that warrant discussion. First, as a technical development work, we did not include patients with ICD implantation. A thorough investigation of safety and effectiveness in patients with ICD implantation is beyond the scope of this work. As such, we are unable to definitively claim that wideband AIR is insensitive to implanted ICD including intracardiac leads. Our phantom study (see Figure 3) shows that intra-cardiac leads do not produce significant image artifacts. Furthermore, our experience with LGE MRI (with a standard hyperbolic secant inversion pulse with frequency bandwidth ~ 1 kHz) in patients with ICDs suggests that the center frequency shift induced by intracardiac leads is not high enough to influence the efficacy of a standard hyperbolic secant inversion pulse. Our experience is consistent with wideband LGE MRI results reported by Rashid et al. (27). The mimicking approach (taping an ICD generator on the subject's left shoulder) was first established by Rashid et al. at 1.5T (27) and verified by our group at 3T (29). Thus, results from this study are likely to translate to patients with ICD implantation. Not testing the performance of wideband AIR cardiac $T_1$ mapping in patients with ICD implantation is a limitation of this study; on the other hand, the proposed study design, with original AIR $T_1$ mapping without ICD as the control, allows reference measurements and repeated measurements without safety concerns associated with lead tip heating. This technical development work may set the foundation for future studies aim at evaluating both the effectiveness and safety of wideband AIR cardiac $T_1$ mapping in patients with implanted cardiac devices. Second, in this study we used a protocol to produce nominal spatial resolution of 2.8 mm × 2.8 mm (4.2 mm × 3.6 mm accounting for the additional blurring caused by Hanning window), in order to compensate for low signal-to-noise ratio. Compared with 3-3-5 MOLLI, wideband AIR is expected to produce lower signal-to-noise ratio (see standard deviation values in Table 1) due to the following factors: b-SSFP (MOLLI) vs. TurboFLASH (wideband AIR), inversion recovery (MOLLI) vs. saturation recovery (wideband AIR), and 11 images (MOLLI) vs. 2 images (wideband AIR). The resolution used in this study will be sensitive to partial volume effects and introduce errors when quantifying $T_1$ from small myocardial lesions. Fortunately, the spatial resolution reported in this study may be adequate for quantifying diffuse cardiac fibrosis in patients with non-ischemic cardiomyopathy. Potential approaches to improve the spatial resolution include the use of dedicated cardiac coil array and image denoising with nonlinear iterative method such as non-local means (49). Third, this study included only one subject with contrast agent administration. Consistent with the BISTRO design (see Appendix), our phantom study (see Table 1) shows that wideband saturation pulse module is insensitive to $T_2$. While both theoretical and in vitro results suggest insensitivity to $T_2$, additional human subjects with contrast agent administration need to be examined to verify that wideband is insensitive to clinically relevant $T_2$.

In summary, this study demonstrates the feasibility of wideband AIR pulse sequence for cardiac $T_1$ mapping without significant image artifacts induced by ICD. A future study of a high number of patients with ICD implantation is warranted to evaluate the clinical utility of wideband AIR cardiac $T_1$ mapping for assessment of myocardial fibrosis burden without image artifacts induced by ICD. This new cardiac-device-insensitive MRI pulse sequence may have a broad impact on cardiac imaging, because it has the potential to activate new clinical studies aimed at advancing other cardiac devices such as biventricular pacemaker.

## Supplementary Material

Refer to Web version on PubMed Central for supplementary material.

## Acknowledgments

## References

1. Go AS, Mozaffarian D, Roger VL, Benjamin EJ, Berry JD, Borden WB, Bravata DM, Dai S, Ford ES, Fox CS, Franco S, Fullerton HJ, Gillespie C, Hailpern SM, Heit JA, Howard VJ, Huffman MD, Kissela BM, Kittner SJ, Lackland DT, Lichtman JH, Lisabeth LD, Magid D, Marcus GM, Marelli A, Matchar DB, McGuire DK, Mohler ER, Moy CS, Mussolino ME, Nichol G, Paynter NP, Schreiner PJ, Sorlie PD, Stein J, Turan TN, Virani SS, Wong ND, Woo D, Turner MB. Heart disease and stroke statistics--2013 update: a report from the American Heart Association. Circulation. 2013; 127(1):e6–e245. [PubMed: 23239837]

2. Yancy CW, Jessup M, Bozkurt B, Butler J, Casey DE, Drazner MH, Fonarow GC, Geraci SA, Horwich T, Januzzi JL, Johnson MR, Kasper EK, Levy WC, Masoudi FA, McBride PE, McMurray JJV, Mitchell JE, Peterson PN, Riegel B, Sam F, Stevenson LW, Tang WHW, Tsai EJ, Wilkoff BL. 2013 ACCF/AHA Guideline for the Management of Heart FailureA Report of the American College of Cardiology Foundation/American Heart Association Task Force on Practice Guidelines. Journal of the American College of Cardiology. 2013; 62(16):e147–e239. [PubMed: 23747642]

3. Simmons A, Tofts PS, Barker GJ, Arridge SR. Sources of intensity nonuniformity in spin echo images at 1.5 T. Magn Reson Med. 1994; 32(1):121–8. [PubMed: 8084227]

4. Greenman RL, Shirosky JE, Mulkern RV, Rofsky NM. Double inversion black-blood fast spin-echo imaging of the human heart: a comparison between 1.5T and 3.0T. J Magn Reson Imaging. 2003; 17(6):648–55. [PubMed: 12766893]

5. Hunt SA, Abraham WT, Chin MH, Feldman AM, Francis GS, Ganiats TG, Jessup M, Konstam MA, Mancini DM, Michl K, Oates JA, Rahko PS, Silver MA, Stevenson LW, Yancy CW. 2009 Focused update incorporated into the ACC/AHA 2005 Guidelines for the Diagnosis and Management of Heart Failure in Adults A Report of the American College of Cardiology Foundation/American Heart Association Task Force on Practice Guidelines Developed in Collaboration With the International Society for Heart and Lung Transplantation. J Am Coll Cardiol. 2009; 53(15):e1–e90. [PubMed: 19358937]

6. Mann DL, Barger PM, Burkhoff D. Myocardial recovery and the failing heart: myth, magic, or molecular target? J Am Coll Cardiol. 2012; 60(24):2465–72. [PubMed: 23158527]

7. Taylor DO, Edwards LB, Aurora P, Christie JD, Dobbels F, Kirk R, Rahmel AO, Kucheryavaya AY, Hertz MI. Registry of the International Society for Heart and Lung Transplantation: twenty-fifth official adult heart transplant report--2008. J Heart Lung Transplant. 2008; 27(9):943–56. [PubMed: 18765186]

8. Zafeiridis A, Jeevanandam V, Houser SR, Margulies KB. Regression of cellular hypertrophy after left ventricular assist device support. Circulation. 1998; 98(7):656–62. [PubMed: 9715858]

9. Slaughter MS, Rogers JG, Milano CA, Russell SD, Conte JV, Feldman D, Sun B, Tatooles AJ, Delgado RM 3rd, Long JW, Wozniak TC, Ghumman W, Farrar DJ, Frazier OH. Advanced heart failure treated with continuous-flow left ventricular assist device. N Engl J Med. 2009; 361(23): 2241–51. [PubMed: 19920051]

10. Russo MJ, Hong KN, Davies RR, Chen JM, Sorabella RA, Ascheim DD, Williams MR, Gelijns AC, Stewart AS, Argenziano M, Naka Y. Posttransplant survival is not diminished in heart transplant recipients bridged with implantable left ventricular assist devices. J Thorac Cardiovasc Surg. 2009; 138(6):1425–32. e1–3. [PubMed: 19931672]

11. Miller LW, Pagani FD, Russell SD, John R, Boyle AJ, Aaronson KD, Conte JV, Naka Y, Mancini D, Delgado RM, MacGillivray TE, Farrar DJ, Frazier OH. Use of a continuous-flow device in patients awaiting heart transplantation. N Engl J Med. 2007; 357(9):885–96. [PubMed: 17761592]

12. Rose EA, Gelijns AC, Moskowitz AJ, Heitjan DF, Stevenson LW, Dembitsky W, Long JW, Ascheim DD, Tierney AR, Levitan RG, Watson JT, Meier P, Ronan NS, Shapiro PA, Lazar RM, Miller LW, Gupta L, Frazier OH, Desvigne-Nickens P, Oz MC, Poirier VL. Long-term use of a left ventricular assist device for end-stage heart failure. N Engl J Med. 2001; 345(20):1435–43. [PubMed: 11794191]

13. Holman WL, Kormos RL, Naftel DC, Miller MA, Pagani FD, Blume E, Cleeton T, Koenig SC, Edwards L, Kirklin JK. Predictors of death and transplant in patients with a mechanical circulatory support device: a multi-institutional study. J Heart Lung Transplant. 2009; 28(1):44–50. [PubMed: 19134530]

14. Kim RJ, Wu E, Rafael A, Chen EL, Parker MA, Simonetti O, Klocke FJ, Bonow RO, Judd RM. The use of contrast-enhanced magnetic resonance imaging to identify reversible myocardial dysfunction. N Engl J Med. 2000; 343(20):1445–53. [PubMed: 11078769]

15. Kramer CM, Chandrashekhar Y, Narula J. T1 mapping by CMR in cardiomyopathy: a noninvasive myocardial biopsy? JACC Cardiovasc Imaging. 2013; 6(4):532–4. [PubMed: 23579019]

16. Iles L, Pfluger H, Phrommintikul A, Cherayath J, Aksit P, Gupta SN, Kaye DM, Taylor AJ. Evaluation of diffuse myocardial fibrosis in heart failure with cardiac magnetic resonance contrast-enhanced T1 mapping. J Am Coll Cardiol. 2008; 52(19):1574–80. [PubMed: 19007595]

17. Sibley CT, Noureldin RA, Gai N, Nacif MS, Liu S, Turkbey EB, Mudd JO, van der Geest RJ, Lima JA, Halushka MK, Bluemke DA. T1 Mapping in Cardiomyopathy at Cardiac MR: Comparison with Endomyocardial Biopsy. Radiology. 2012; 265(3):724–32. [PubMed: 23091172]

18. Miller CA, Naish JH, Bishop P, Coutts G, Clark D, Zhao S, Ray SG, Yonan N, Williams SG, Flett AS, Moon JC, Greiser A, Parker GJ, Schmitt M. Comprehensive validation of cardiovascular magnetic resonance techniques for the assessment of myocardial extracellular volume. Circ Cardiovasc Imaging. 2013; 6(3):373–83. [PubMed: 23553570]

19. Flett AS, Hayward MP, Ashworth MT, Hansen MS, Taylor AM, Elliott PM, McGregor C, Moon JC. Equilibrium contrast cardiovascular magnetic resonance for the measurement of diffuse myocardial fibrosis: preliminary validation in humans. Circulation. 2010; 122(2):138–44. [PubMed: 20585010]

20. Kehr E, Sono M, Chugh SS, Jerosch-Herold M. Gadolinium-enhanced magnetic resonance imaging for detection and quantification of fibrosis in human myocardium in vitro. Int J Cardiovasc Imaging. 2008; 24(1):61–8. [PubMed: 17429755]

21. Jerosch-Herold M, Sheridan DC, Kushner JD, Nauman D, Burgess D, Dutton D, Alharethi R, Li D, Hershberger RE. Cardiac magnetic resonance imaging of myocardial contrast uptake and blood flow in patients affected with idiopathic or familial dilated cardiomyopathy. Am J Physiol Heart Circ Physiol. 2008; 295(3):H1234–H42. [PubMed: 18660445]

22. White SK, Sado DM, Fontana M, Banypersad SM, Maestrini V, Flett AS, Piechnik SK, Robson MD, Hausenloy DJ, Sheikh AM, Hawkins PN, Moon JC. T1 mapping for myocardial extracellular volume measurement by CMR: bolus only versus primed infusion technique. JACC Cardiovasc Imaging. 2013; 6(9):955–62. [PubMed: 23582361]

23. Arheden H, Saeed M, Higgins CB, Gao DW, Bremerich J, Wyttenbach R, Dae MW, Wendland MF. Measurement of the distribution volume of gadopentetate dimeglumine at echo-planar MR imaging to quantify myocardial infarction: comparison with 99mTc-DTPA autoradiography in rats. Radiology. 1999; 211(3):698–708. [PubMed: 10352594]

24. Moon JC, Messroghli DR, Kellman P, Piechnik SK, Robson MD, Ugander M, Gatehouse PD, Arai AE, Friedrich MG, Neubauer S, Schulz-Menger J, Schelbert EB. Myocardial T1 mapping and extracellular volume quantification: a Society for Cardiovascular Magnetic Resonance (SCMR) and CMR Working Group of the European Society of Cardiology consensus statement. J Cardiovasc Magn Reson. 2013; 15(1):92. [PubMed: 24124732]

25. Sommer T, Naehle CP, Yang A, Zeijlemaker V, Hackenbroch M, Schmiedel A, Meyer C, Strach K, Skowasch D, Vahlhaus C, Litt H, Schild H. Strategy for safe performance of extrathoracic magnetic resonance imaging at 1.5 tesla in the presence of cardiac pacemakers in non-pacemaker-

dependent patients: a prospective study with 115 examinations. Circulation. 2006; 114(12):1285–92. [PubMed: 16966587]

26. Nazarian S, Roguin A, Zviman MM, Lardo AC, Dickfeld TL, Calkins H, Weiss RG, Berger RD, Bluemke DA, Halperin HR. Clinical utility and safety of a protocol for noncardiac and cardiac magnetic resonance imaging of patients with permanent pacemakers and implantable-cardioverter defibrillators at 1.5 tesla. Circulation. 2006; 114(12):1277–84. [PubMed: 16966586]

27. Rashid S, Rapacchi S, Vaseghi M, Tung R, Shivkumar K, Finn JP, Hu P. Improved late gadolinium enhancement MR imaging for patients with implanted cardiac devices. Radiology. 2014; 270(1):269–74. [PubMed: 24086074]

28. Stevens SM, Tung R, Rashid S, Gima J, Cote S, Pavez G, Khan S, Ennis DB, Finn JP, Boyle N, Shivkumar K, Hu P. Device artifact reduction for magnetic resonance imaging of patients with implantable cardioverter-defibrillators and ventricular tachycardia: late gadolinium enhancement correlation with electroanatomic mapping. Heart Rhythm. 2014; 11(2):289–98. [PubMed: 24140812]

29. Ranjan R, McGann CJ, Jeong EK, Hong K, Kholmovski EG, Blauer J, Wilson BD, Marrouche NF, Kim D. Wideband late gadolinium enhanced magnetic resonance imaging for imaging myocardial scar without image artefacts induced by implantable cardioverter-defibrillator: a feasibility study at 3 T. Europace. 2014

30. Fitts M, Breton E, Kholmovski EG, Dosdall DJ, Vijayakumar S, Hong KP, Ranjan R, Marrouche NF, Axel L, Kim D. Arrhythmia insensitive rapid cardiac T1 mapping pulse sequence. Magn Reson Med. 2013; 70(5):1274–82. [PubMed: 23280998]

31. Kim D, Oesingmann N, McGorty K. Hybrid adiabatic-rectangular pulse train for effective saturation of magnetization within the whole heart at 3 T. Magn Reson Med. 2009; 62(6):1368–78. [PubMed: 19785021]

32. Luo Y, de Graaf RA, DelaBarre L, Tannus A, Garwood M. BISTRO: an outer-volume suppression method that tolerates RF field inhomogeneity. Magn Reson Med. 2001; 45(6):1095–102. [PubMed: 11378888]

33. Kellman P, Herzka DA, Hansen MS. Adiabatic inversion pulses for myocardial T1 mapping. Magn Reson Med. 2014; 71(4):1428–34. [PubMed: 23722695]

34. Griswold MA, Jakob PM, Heidemann RM, Nittka M, Jellus V, Wang J, Kiefer B, Haase A. Generalized autocalibrating partially parallel acquisitions (GRAPPA). Magn Reson Med. 2002; 47(6):1202–10. [PubMed: 12111967]

35. Breton E, Kim D, Chung S, Axel L. Quantitative contrast-enhanced first-pass cardiac perfusion MRI at 3 tesla with accurate arterial input function and myocardial wall enhancement. J Magn Reson Imaging. 2011; 34(3):676–84. [PubMed: 21761467]

36. Chung S, Kim D, Breton E, Axel L. Rapid B1+ mapping using a preconditioning RF pulse with TurboFLASH readout. Magn Reson Med. 2010; 64(2):439–46. [PubMed: 20665788]

37. Costantini M. A novel phase unwrapping method based on network programming. IEEE Transactions on Geoscience and Remote Sensing. 1998; 36(3):813–21.

38. Ulmer JL, Mathews VP, Hamilton CA, Elster AD, Moran PR. Magnetization transfer or spin-lock? An investigation of off-resonance saturation pulse imaging with varying frequency offsets. American Journal of Neuroradiology. 1996; 17(5):805–19. [PubMed: 8733952]

39. Messroghli DR, Radjenovic A, Kozerke S, Higgins DM, Sivananthan MU, Ridgway JP. Modified Look-Locker inversion recovery (MOLLI) for high-resolution T1 mapping of the heart. Magn Reson Med. 2004; 52(1):141–6. [PubMed: 15236377]

40. Kim D, Jensen JH, Wu EX, Sheth SS, Brittenham GM. Breathhold multiecho fast spin-echo pulse sequence for accurate R2 measurement in the heart and liver. Magn Reson Med. 2009; 62(2):300–6. [PubMed: 19526516]

41. Stanisz GJ, Odrobina EE, Pun J, Escaravage M, Graham SJ, Bronskill MJ, Henkelman RM. T1, T2 relaxation and magnetization transfer in tissue at 3T. Magn Reson Med. 2005; 54(3):507–12. [PubMed: 16086319]

42. Chow K, Flewitt JA, Green JD, Pagano JJ, Friedrich MG, Thompson RB. Saturation recovery single-shot acquisition (SASHA) for myocardial T(1) mapping. Magn Reson Med. 2014; 71(6):2082–95. [PubMed: 23881866]

43. Buckland JR, Huntley JM, Turner SRE. Unwrapping noisy phase maps by use of a minimum-cost-matching algorithm. Applied Optics. 1995; 34(23):5100–8. [PubMed: 21052355]

44. Nordbeck P, Fidler F, Friedrich MT, Weiss I, Warmuth M, Gensler D, Herold V, Geistert W, Jakob PM, Ertl G, Ritter O, Ladd ME, Bauer WR, Quick HH. Reducing RF-related heating of cardiac pacemaker leads in MRI: implementation and experimental verification of practical design changes. Magn Reson Med. 2012; 68(6):1963–72. [PubMed: 22383393]

45. Piechnik SK, Ferreira VM, Dall'Armellina E, Cochlin LE, Greiser A, Neubauer S, Robson MD. Shortened Modified Look-Locker Inversion recovery (ShMOLLI) for clinical myocardial T1-mapping at 1.5 and 3 T within a 9 heartbeat breathhold. J Cardiovasc Magn Reson. 2010; 12:69. [PubMed: 21092095]

46. Song T, Stainsby JA, Ho VB, Hood MN, Slavin GS. Flexible cardiac T1 mapping using a modified Look-Locker acquisition with saturation recovery. Magn Reson Med. 2012; 67(3):622–7. [PubMed: 22344580]

47. Reeder SB, Faranesh AZ, Boxerman JL, McVeigh ER. In vivo measurement of T*2 and field inhomogeneity maps in the human heart at 1.5 T. Magn Reson Med. 1998; 39(6):988–98. [PubMed: 9621923]

48. Kim D, Cernicanu A, Axel L. B(0) and B(1)-insensitive uniform T(1)-weighting for quantitative, first-pass myocardial perfusion magnetic resonance imaging. Magn Reson Med. 2005; 54(6): 1423–9. [PubMed: 16254944]

49. Coupe P, Yger P, Barillot C. Fast non local means denoising for 3D MR images. Med Image Comput Comput Assist Interv. 2006; 9(Pt 2):33–40. [PubMed: 17354753]

50. Kim D, Gonen O, Oesingmann N, Axel L. Comparison of the effectiveness of saturation pulses in the heart at 3T. Magn Reson Med. 2008; 59(1):209–15. [PubMed: 18050347]

## Appendix

## BISTRO Implementation Details

We implemented BISTRO as a train of 15 hyperbolic secant adiabatic inversion RF pulses, with crusher gradients in between RF pulses to minimize stimulated echoes, and spoiler gradients before the first RF pulse and after the last RF pulse to dephase the transverse magnetization (see Figure 1). We decreased the duration from the first to last set of crusher gradients to suppress stimulated echoes. The total duration, including crusher and spoiler gradients, was 151 ms. Each hyperbolic secant inversion pulse (frequency modulation parameter $\beta = 750$ radians/s, phase modulation parameter $\mu = 10$ [dimensionless]) was 3.07 ms long and its nominal transmit $B_1+$ (normalized by gyromagnetic ratio) calibrated by the transmit body coil was 926 Hz. The number of pulses and nominal $B_1+$ (i.e., amplitude) for each pulse were empirically determined in a preliminary phantom experiment, where we systematically adjusted the number of RF pulses and nominal $B_1+$ to consistently achieve effective saturation of magnetization (i.e., residual $M_z$ immediately after the last RF pulse in the module is less than 5% of equilibrium magnetization ($M_0$)).

## Calculation of Frequency Bandwidth of the Saturation Pulse Modules

We determined empirically, in a phantom positioned near magnet isocenter, the frequency bandwidth of the original and wideband saturation modules. Using the approach described in (31, 48, 50), we quantified the residual $M_z$ immediately after the saturation pulse module, by normalizing the saturation-no-recovery image (i.e., TD = 3 ms, which is the duration of the spoiler gradients) with the PD image (i.e., $M_0$) and calculating the residual $M_z$ as a fraction of $M_0$ (0 to 1). Note that residual $M_z$ of 0 corresponds to complete saturation of

magnetization, whereas residual $M_z$ of 1 corresponds to no rotation. The experiment was repeated by adjusting the center frequency offset of the saturation pulse module from −6 to 6 kHz (variable steps). We then plotted the residual $M_z$ (as a fraction of $M_0$) as a function of center frequency shift to calculate the FWHM, which is by definition the frequency bandwidth of the saturation pulse module. As shown in Figure 2, the residual $M_z$ curve for original saturation pulse module had side lobes. This observation is consistent with the fact that original saturation pulse module is comprised of 3 rectangular RF pulses (i.e., Fourier transform of a rectangular function is a sinc; see Figure 2).
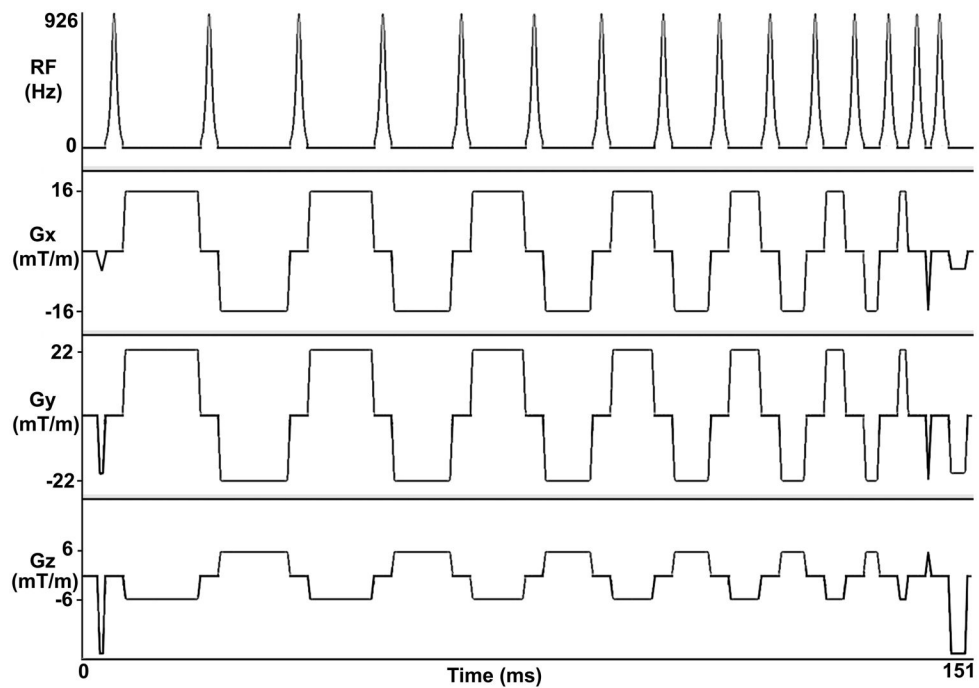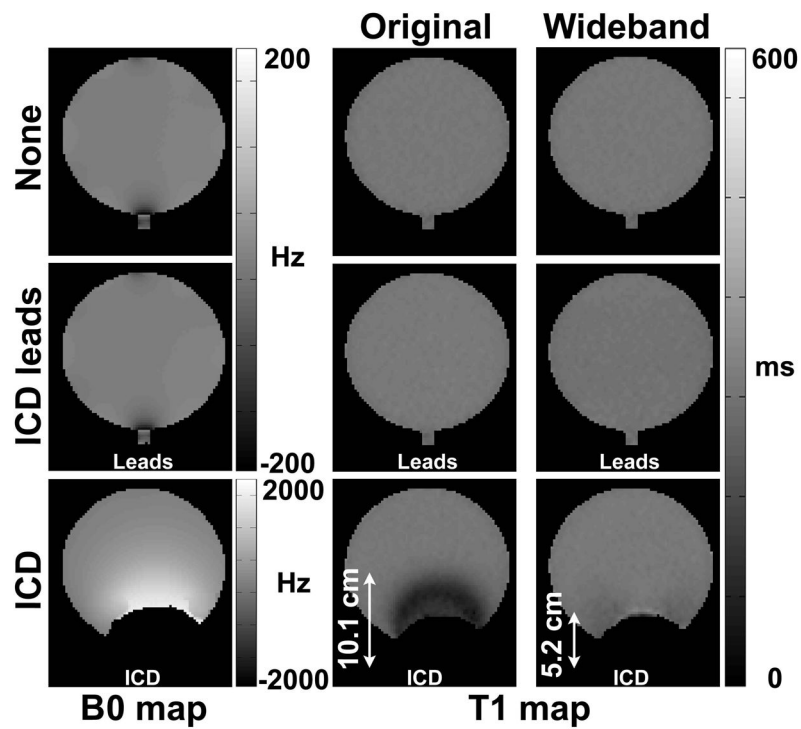
**Figure 1.**
Pulse sequence diagram of a wideband saturation pulse module (BISTRO), which is comprised of 15 hyperbolic secant inversion RF pulses that do not meet the adiabatic condition on purpose. The spoiler gradients are applied before the first RF pulse and after the last RF pulse to dephase the transverse magnetization. The crusher gradients in between RF pulses are played to minimize stimulated echoes. While duration of the wideband saturation pulse module is 151 ms, the total RF time is only 46.05 ms, whereas the remaining time is used to play crusher and spoiler magnetic field gradients. These diagrams are drawn to approximate proportions but not to exact scale. $G_z$: slice-select gradient; $G_y$: phase-encoding gradient; $G_x$: frequency-encoding gradient.
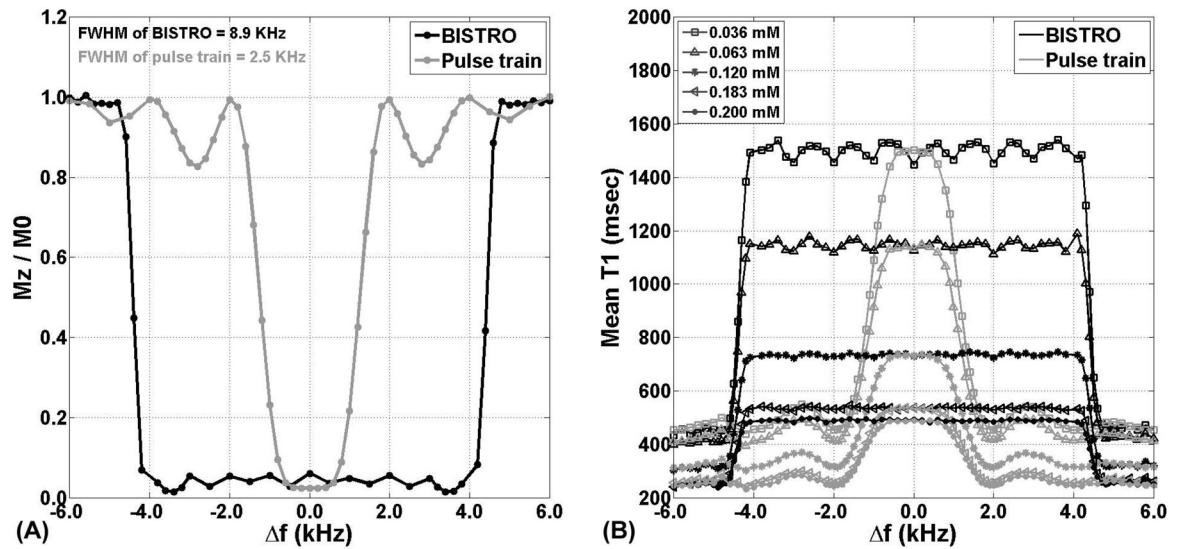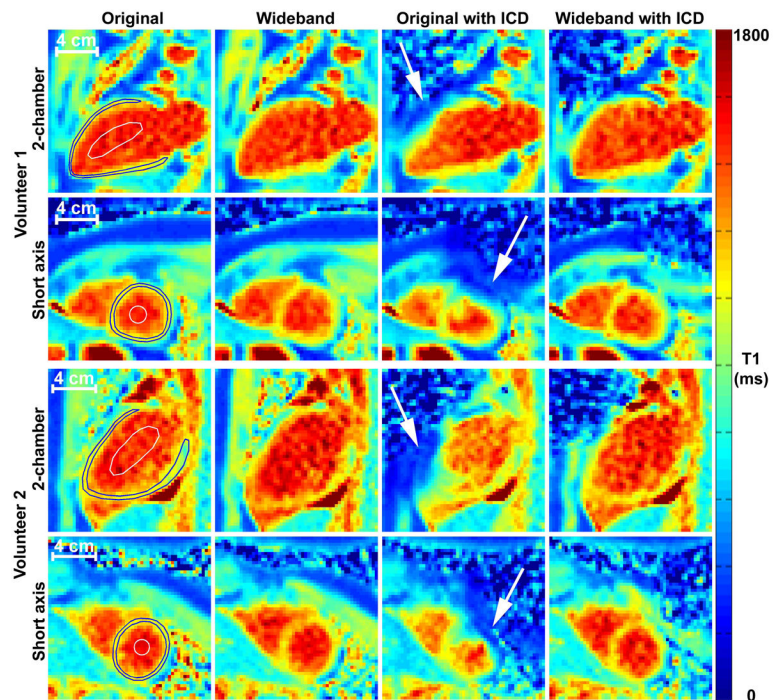
**Figure 2.**
(A) Plots of residual $M_z$ (as a fraction of $M_0$) as a function of center frequency shift. Note that residual $M_z = 0$ corresponds to complete saturation of magnetization, whereas residual $M_z = 1$ corresponds to no saturation. Compared with the original saturation pulse module (gray line), wideband pulse module (black line) had 256% higher frequency bandwidth (FWHM = 2.5 kHz and 8.9 kHz for original and wideband, respectively). f = center frequency shift. (B) Plots of $T_1$ as a function of center frequency shift. Consistent with the frequency bandwidth experiment, wideband AIR (black line) produced consistent $T_1$ results over 8.9 kHz, whereas original AIR (gray line) produced consistent $T_1$ results over 2.5 kHz.
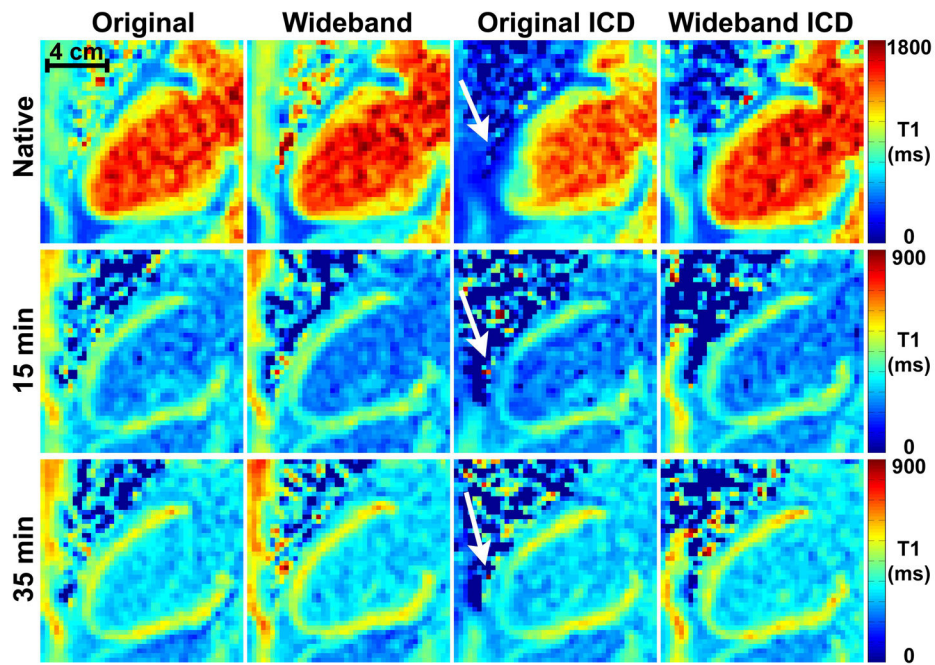
**Figure 3.**
Coronal $T_1$ maps of a phantom acquired with original AIR (middle column) and wideband AIR (right column): without anything taped (top row), with ICD leads (middle row), and with ICD taped on one side of the phantom as shown (bottom row). The corresponding $B_0$ maps are also shown (left column). Regions near the ICD were removed because of significant signal dropout. Arrows display the distance between ICD and outer boundary of the contaminated region.

**Figure 4.**
Representative native $T_1$ maps in short-axis (rows 2 and 4) and long-axis (rows 1 and 3) planes of the heart of two different volunteers with and without ICD taped on their left shoulder (~5–10 cm from the heart): original AIR without ICD (column 1), wideband AIR without ICD (column 2), original AIR with ICD (column 3), and wideband AIR with ICD (column 4). Compared with original AIR without ICD as the control, original AIR with ICD produced less accurate $T_1$ results, whereas wideband AIR with ICD produced more accurate $T_1$ results. White arrows point to cardiac regions compromised by ICD. Blood and cardiac contours superimposed on the left column only. See Supporting Table S1 for the corresponding $T_1$ values.

**Figure 5.**

Representative native and post-contrast (15 and 35 min after MultiHance administration) $T_1$ maps in a 2-chamber plane of the heart acquired with and without ICD taped on his left shoulder (~5–10 cm from the heart): original AIR without ICD (column 1), wideband AIR without ICD (column 2), original AIR with ICD (column 3), and wideband AIR with ICD (column 4). Compared with original AIR without ICD as the control, original AIR with ICD produced less accurate $T_1$ results, whereas wideband AIR with ICD produced more accurate $T_1$ results. White arrows point to cardiac regions compromised by ICD. See Supporting Table S2 for the corresponding $T_1$ values.

**Table 1**

Summary of $T_1$ measurements of five $MnCl_2$ phantoms representing native myocardium (1,174 ms) and blood (1,550 ms) and post-contrast (500, 549, and 755 ms) blood/tissue $T_1$ values.

| $MnCl_2$ (mM) | $T_2$ (ms) | IR-FSE (ms) | 3-3-5 MOLLI (ms) | Original AIR (ms) | Wideband AIR (ms) | Original AIR with ICD (ms) | Wideband AIR with ICD (ms) |
|---|---|---|---|---|---|---|---|
| 0.036 | 294 | 1550 ± 20 | 1503 ± 13 (−3.1%) | 1525 ± 78 (−1.7%) | 1493 ± 79 (−3.7%) | 743 ± 265 (−52.1%) | 1546 ± 88 (−0.3%) |
| 0.063 | 184 | 1174 ± 15 | 1160 ± 10 (−1.2%) | 1197 ± 52 (1.9%) | 1158 ± 59 (−1.3%) | 643 ± 198 (−45.2%) | 1142 ± 55 (−2.8%) |
| 0.120 | 101 | 755 ± 11 | 761 ± 9 (0.8%) | 752 ± 31 (−0.4%) | 740 ± 27 (−2.0%) | 479 ± 120 (−36.6%) | 760 ± 29 (0.6%) |
| 0.183 | 69 | 549 ± 9 | 545 ± 13 (−0.8%) | 547 ± 25 (−0.5%) | 525 ± 26 (−4.4%) | 385 ± 83 (−30.0%) | 551 ± 25 (0.2%) |
| 0.200 | 62 | 500 ± 7 | 497 ± 6 (−0.5%) | 495 ± 23 (−1.0%) | 479 ± 20 (−4.1%) | 355 ± 65 (−29.0%) | 475 ± 24 (−4.9%) |

Values represent mean ± standard deviation within an ROI. Percent error (relative to IR-FSE without ICD) is reported in parenthesis. Note that the standard deviation within an ROI is larger for original AIR with ICD than the other three AIR acquisitions (original AIR without ICD, wideband AIR without ICD, and wideband AIR with ICD).

## Table 2

Summary of mean myocardial and blood $T_1$ measurements over 11 human subjects. These $T_1$ measurements were made with original AIR without ICD, wideband AIR without ICD, original AIR with ICD, and wideband AIR with ICD.

| Tissue Type | Original (ms) | Wideband (ms) | Original with ICD (ms) | Wideband with ICD (ms) |
|---|---|---|---|---|
| 2-CH, Myocardium | 1093.6 ± 42.1 | 1158.8 ± 44.5 (6.0%) | *884.8 ± 84.8 (−19.1%) | 1114.9 ± 68.8 (2.0%) |
| SAX, Myocardium | 1069.8 ± 29.3 | 1137.7 ± 28.6 (6.4%) | *837.9 ± 115.8 (−21.7%) | 1091.4 ± 82.7 (2.0%) |
| 2-CH, Blood | 1470.0 ± 75.3 | 1498.3 ± 57.6 (1.9%) | *1321.6 ± 124.7 (−10.1%) | 1489.7 ± 60.8 (1.3%) |
| SAX, Blood | 1473.9 ± 89.2 | 1522.5 ± 52.3 (3.3%) | *1241.0 ± 268.9 (−15.8%) | 1496.6 ± 58.3 (1.5%) |

Values represent mean ± standard deviation over 11 subjects. Percent error (relative to original AIR without ICD) is reported in parenthesis. Myocardial $T_1$ was significantly ($p < 0.001$) different between four acquisitions in 2-chamber and short-axis planes. Compared with original AIR without ICD as the control, only original AIR with ICD was significantly different in both imaging planes ($p < 0.05$). The same trends were observed for blood $T_1$ (ANOVA; $p < 0.001$), where only original AIR with ICD (column 4) was significantly different from original AIR without ICD in both imaging planes ($p < 0.05$). We regret that the Analyse-it software does not report the adjusted p values for the Bonferroni paired-wise test. 2-CH: 2-chamber view; SAX: short-axis view.

*
 $p < 0.05$ with respect to original AIR without ICD as the control.